



Horizontal continuous casting process under electromagnetic field for preparing AA3003/AA4045 clad composite hollow billets

Li WU¹, Hui-jun KANG², Zong-ning CHEN², Ning LIU¹, Tong-min WANG¹

1. Key Laboratory of Materials Modification by Laser, Ion and Electron Beams (Ministry of Education), School of Materials Science and Engineering, Dalian University of Technology, Dalian 116024, China;
2. Laboratory of Special Processing of Raw Materials, Dalian University of Technology, Dalian 116024, China

Received 24 October 2014; accepted 17 March 2015

Abstract: A modified horizontal continuous casting process under the electromagnetic field was proposed for preparing AA3003/AA4045 clad composite hollow billets. To investigate the effect of electromagnetic field on this process, a comprehensive three-dimensional model was developed. Two cases with and without electromagnetic field were compared using the simulations. When rotating electromagnetic stirring is applied, the flow pattern of fluid melt is greatly modified; the mushy zone becomes much wider, the temperature profile becomes more uniform, and the solid fraction decreases for both the external and internal alloy melt layers. These modifications are beneficial for the formation of a bimetal interface and fine and uniform grain structure of the clad composite hollow billet. Experiments conducted using the same electrical and casting parameters as the simulations verify that under the electromagnetic field the microstructure of the clad composite hollow billet becomes fine and the diffusion of the elements at the interface is promoted.

Key words: aluminum alloy; clad composite; hollow billet; horizontal continuous casting; electromagnetic stirring; numerical simulation

1 Introduction

Aluminum clad composite products exhibit an excellent combination of physical, chemical and mechanical properties that cannot be achieved by a monolithic material. These materials have been successfully used in the automotive and other industries. For example, some radiators and heat exchangers are manufactured with the AA4045/AA3003 clad brazing products which are made from a thin clad layer of the AA4045 brazing alloy clad onto the corrosion-resistant AA3003 alloy. Double performances can thus be improved for not only the weldability but also the corrosion resistance.

The conventional method for cladding products involves roll bonding or welding [1–4]. Although the roll bonding method has served the industry well for decades, this approach still has some practical issues. A major disadvantage is that roll bonding is a very time intensive

and expensive process and it is impossible to remove all of the oxides at the interface [5].

Recently, the process of simultaneous casting has been developed for the manufacturing of clad composite slabs, rods or tubes [6–11]. This casting process has distinct advantages of both cost reduction and interface improvement. In addition, the use of an electromagnetic field, which can significantly improve the solidification structure and mechanical properties of billets [12–15], has gained wide application in the metallurgy industry due to the advantages of the high energy density and controllability of this non-contact technique.

In order to understand the casting process under electromagnetic field, numerical modeling is used increasingly by many researchers with the development of powerful numerical methods and computers. Several models were developed to analyze fluid flow, heat and mass transfer and solidification during the casting process [16–22]. For instance, BASERINIA et al [21] developed a steady-state thermofluids model of the

Foundation item: Projects (51274054, U1332115, 51271042, 51375070, 51401044) supported by the National Natural Science Foundation of China; Project (313011) supported by the Key Grant Project of Ministry of Education of China; Project (2013A16GX110) supported by the Science and Technology Planning Project of Dalian, China; Project (2014M551075) supported by the China Postdoctoral Science Foundation; Project supported by the Fundamental Research Funds for the Central Universities, China

Corresponding author: Tong-min WANG; Tel: +86-411-84706790; E-mail: tmwang@dlut.edu.cn
DOI: 10.1016/S1003-6326(15)63891-2

fusion co-casting technology casting process to simulate the casting of rectangular bimetallic ingots. FOROOZMEHR et al [22] described a coupled dissolution and diffusion model of solutionizing and solute redistribution in a co-cast bi-layer aluminum alloy system. NASTAC and STEFANESCU [17] developed a general stochastic model to describe the fraction of solid evolution, cooling curves and microstructure formation in castings. In addition, numerous scholars focused on the effects of an electromagnetic field on the fluid flow or solidification during the casting process using numerical simulations [23–29]. For example, ZHANG et al [26] developed a comprehensive mathematical model to describe the interaction of the multiple physics fields during low frequency electromagnetic casting of 7xxx aluminum alloys. LI et al [28] performed a simulation study on the horizontal continuous casting process of copper hollow billets under rotating electromagnetic stirring. CHAUDHARY et al [29] investigated the effect of static electromagnetic braking on the transient turbulent flow in continuous slab casting using large eddy simulations.

Based on the work by LIU et al [11,30], rotating electromagnetic stirring (REMS) was applied to the horizontal continuous casting process for preparing clad aluminum hollow billets. However, few studies have been reported, which investigated the casting process for manufacturing clad composite hollow billets under an electromagnetic field using numerical simulations. In this work, a comprehensive three-dimensional numerical simulation model was developed to investigate the solidification process of clad composite hollow billets during horizontal continuous casting under rotating electromagnetic stirring. The effects of rotating electromagnetic stirring on the flow field and thermal field were studied using this model. Corresponding experiments were implemented to verify the simulation work.

2 Experimental

The schematic of the experimental apparatus, presented in Fig. 1, contains the tundish, crystallizer, water-cooling system, withdrawal device and electromagnetic system. The crystallizer is composed of an annular baffle plate, a graphite mold consisting of an inner mold and an exterior mold, and a water-cooling copper outer-jacket. The annular baffle plate is fixed into the graphite mold between the molten alloys. A three-phase rotating electromagnetic stirrer, with 6 poles and 42 turns per winding, as shown in Fig. 2(a), is installed around the graphite mold. The power phase difference between adjacent poles is $2/3\pi$. In this experiment, molten metal of the external layer was

poured into the graphite mold from the furnace first. Once the drawing system started working, the melt of the internal layer was poured into the tundish and entered into the central part of the graphite mold through the graphite duct, and then, the combination of internal and external alloys occurred at the bottom of the annular baffle plate. The liquid metal stream was precisely controlled by a flow control tap, and the clad composite hollow billet was continuously withdrawn from the crystallizer. Rotating electromagnetic field stirring was applied during the horizontal continuous casting.

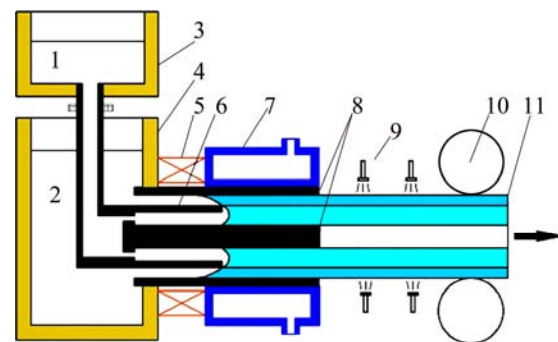


Fig. 1 Schematic of experimental apparatus: 1—AA3003 melt; 2—AA4045 melt; 3—Tundish; 4—Furnace; 5—Electromagnetic stirrer; 6—Annular baffle plate; 7—Water-cooling copper outer-jacket; 8—Graphite mold; 9—Second cooling system; 10—Drawing system; 11—Clad composite hollow billet

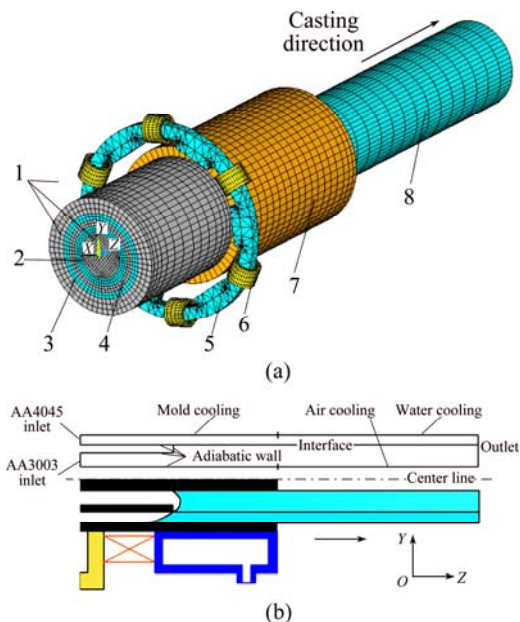


Fig. 2 Computational grid in ANSYS Mechanical (a) and boundary conditions in ANSYS FLUENT (b): 1—Graphite mold; 2—AA3003 melt; 3—AA4045 melt; 4—Annular graphite plate; 5—Iron core of electromagnetic stirrer; 6—Coil winding of electromagnetic stirrer; 7—Water cooling copper outer-jacket; 8—Clad composite hollow billet

3 Simulation model

3.1 Assumptions

To simplify the problem, certain assumptions were made:

- 1) The displacement current is neglected.
- 2) The variety of the fluid field has little effect on the distribution of the magnetic field.
- 3) Joule heat is not considered in this model because the Joule heat produced during the low-frequency electromagnetic casting process is much smaller compared with the entropy inflow with the liquid aluminum with respect to room temperature.
- 4) The molten aluminum alloys behave as incompressible fluids. The effect of liquid surface fluctuations in the flow and the additional magnetic field produced by the flow of aluminum liquid in the mold are ignored.
- 5) The calculation of the solute field is not included in this model and ignores the interface reaction between AA3003 and AA4045 alloys.

3.2 Governing equations

The Maxwell's equations are used for electromagnetic field calculation. The governing equations for flow field and thermal field are described as follows.

Continuity equation:

$$\frac{\partial \rho}{\partial t} + \nabla \cdot (\rho \mathbf{U}) = 0 \quad (1)$$

Momentum equation:

$$\frac{\partial (\rho \mathbf{U})}{\partial t} + \nabla \cdot (\rho \mathbf{U} \mathbf{U}) = \nabla \cdot (\mu_{\text{eff}} \nabla \mathbf{U}) - \nabla p + \frac{f_s^2}{(f_L^3 + \delta)} A_{\text{mush}} (\mathbf{U} - \mathbf{U}_s) - \rho g \beta (T - T_0) + F \quad (2)$$

where \mathbf{U} is the fluid velocity; ρ is the density; μ_{eff} is the effective viscosity coefficient, where $\mu_{\text{eff}} = \mu_l + \mu_t$, μ_l is the laminar viscosity and μ_t is the turbulent viscosity; p is the pressure; f_L and f_S are the liquid and solid volume fractions, respectively; T is the temperature; T_0 is the reference temperature and was assumed to be equal to the liquidus temperature in the current study; δ is a small number to prevent division by zero; A_{mush} is the mushy zone constant; \mathbf{U}_s is the solid velocity due to the pulling of solidified material out of the domain; g is the gravitational acceleration; β is the thermal expansion coefficient of the molten aluminum; and F is the Lorentz force and is ignored during the casting process without REMS. In this model, the lever rule is used to calculate the solid fraction f_S and the liquid fraction f_L , which are functions of temperature and are expressed using the following equations:

$$f_L = \begin{cases} 1, & T \geq T_L \\ 1 - \frac{1}{1 - k_p} \frac{T_L - T}{T_f - T}, & T_S < T < T_L \quad \text{and} \quad f_S = 1 - f_L \\ 0, & T \leq T_S \end{cases} \quad (3)$$

where k_p is the solute partition coefficient, T_f is the fusion temperature of the pure base metal and T_L and T_S are the liquidus and solidus temperatures, respectively.

The standard $k-\varepsilon$ model, which is a semi-empirical model, is used to model the transport of turbulence kinetic energy and its dissipation rate. The first form of this model is

$$\mu_t = \rho C_\mu \frac{k^2}{\varepsilon} \quad (4)$$

where C_μ is a function of the turbulent Reynolds number, which is a constant value, k and ε represent the turbulence kinetic energy and its rate of dissipation, respectively and are obtained using the following transport equations:

$$\frac{\partial (\rho k)}{\partial t} + \nabla \cdot (\rho \mathbf{U} k) = \nabla \cdot \left[\left(\mu_l + \frac{\mu_t}{\sigma_k} \right) \nabla k \right] + G - \rho \varepsilon \quad (5)$$

$$\frac{\partial (\rho \varepsilon)}{\partial t} + \nabla \cdot (\rho \mathbf{U} \varepsilon) = \nabla \cdot \left[\left(\mu_l + \frac{\mu_t}{\sigma_\varepsilon} \right) \nabla \varepsilon \right] + c_1 \frac{\varepsilon}{k} G - c_2 \rho \frac{\varepsilon^2}{k} \quad (6)$$

where μ_l is the laminar viscosity, G represents the generation of turbulence kinetic energy, c_1 and c_2 are constants, σ_k and σ_ε are the turbulent Prandtl numbers for k and ε , respectively. All constants used in Eqs. (4)–(6) are given as follows: $C_\mu=0.09$, $c_1=1.44$, $c_2=1.92$, $\sigma_k=1.0$ and $\sigma_\varepsilon=1.3$.

Energy equation:

$$\frac{\partial (\rho H)}{\partial t} + \nabla \cdot (\rho \mathbf{U} H) = \nabla \cdot (k_T \nabla T) \quad (7)$$

The enthalpy H of the material is computed as the sum of the sensible enthalpy $h = \int_{T_{\text{ref}}}^T c_p dT$ and the latent heat $\Delta H = f_L \Delta H_f$ in the energy equation as

$$H = \int_{T_{\text{ref}}}^T c_p dT + f_L \Delta H_f \quad (8)$$

where k_T is the thermal conductivity, T_{ref} is the reference temperature, c_p is the specific heat capacity at constant pressure, f_L is the liquid volume fraction and ΔH_f is the latent heat of the material. The latent heat is released uniformly between the liquidus and solidus temperatures. In other words, the enthalpy changes linearly over the solidification range.

4 Numerical procedure

The current model was based on a combination of

the commercial software package ANSYS Mechanical and ANSYS FLUENT (Dalian University of Technology is authorized by ANSYS Inc., to use these softwares), with the former for calculation of the electromagnetic field and the latter for calculations of the fluid flow, heat transfer and solidification. When the casting process without REMS was simulated, only the flow field and thermal field were solved. During the REMS process, coupled modeling of the electromagnetic field and other fields must be performed. Moreover, this interaction is in a single direction. That is, the electromagnetic field has an effect on the other fields, while these fields have no effect on the electromagnetic field. The electromagnetic field was first solved using ANSYS Mechanical. Then, the obtained Lorentz force was added to the conservation equation of momentum as the source term while solving the flow field and thermal field in ANSYS FLUENT. Figures 2(a) and (b) present the computational grid and boundary conditions, respectively. The graphite mold and annular baffle plate are 340 mm and 140 mm in length, respectively. The sizes of the clad composite hollow billet are $d86\text{ mm}\times 21\text{ mm}$ with a simulation length of 650 mm. The thicknesses of the internal and external layer of the clad composite hollow billet are 15 mm and 6 mm, respectively.

During the calculation procedure of the

electromagnetic field based on the ANSYS Mechanical, the magnetic vector potential method is used. Furthermore, when other fields are calculated based on ANSYS FLUENT, the pressure–velocity coupling algorithm is the simple algorithm, the difference schemes are the first-order upwind scheme and all of the calculations are run with a time-step of 0.001 s.

4.1 Casting parameters and material properties

In this work, two different casting processes were modeled, and the electrical and casting parameters are listed in Table 1. AA3003 and AA4045 aluminum alloys were used as the experiment materials for the internal and external layers of the clad composite hollow billet, respectively. The chemical composition of AA3003 is 0.219% Si, 1.066% Mn, 0.553% Fe, 0.073% Cu, 0.006% Ti, 0.008% Ni, 0.003% Zn, and the balance is Al. The chemical composition of AA4045 is 9.857% Si, 0.004% Mn, 0.156% Fe, 0.001% Cu, 0.012% Ti, 0.007% Ni, 0.001% Zn, and the balance is Al. The material properties used in this study are listed in Tables 2–4 [31].

4.2 Boundary conditions

When the electromagnetic field was solved, the boundary conditions in the outer air region were set with the magnetic flux parallel condition, and the interface

Table 1 Casting process parameters

Condition	Pouring temperature (AA3003)/K	Pouring temperature (AA4045)/K	Casting speed/ (mm·min ⁻¹)	Electromagnetic frequency/Hz	Current/A
Without REMS	1003	963	120	0	0
With REMS	1003	963	120	50	80

Table 2 Thermo-physical properties of material

Material	Density/ (kg·m ⁻³)	Viscosity/ (kg·m ⁻¹ ·s ⁻¹)	Thermal expansion coefficient/K ⁻¹	Latent heat of fusion/ (kJ·kg ⁻¹)	Solidus temperature/ K	Liquidus temperature/ K	Solute partition coefficient
AA3003	2730	0.00115	2.3×10^{-5}	386	916	927	0.67
AA4045	2657	0.00115	2.1×10^{-5}	460	851	862	0.13

Table 3 Magnetic properties of material

Material	AA3003	AA4045	Copper	Iron core	Coil	Graphite	Air
Electric resistivity/($\Omega\cdot\text{m}$)	4.2×10^{-8}	4.31×10^{-8}	2.92×10^{-8}	7.3×10^{-7}	1.68×10^{-8}	1.42×10^{-5}	–
Relative permeability	1	1	1	10000	1	1	1

Table 4 Specific heat capacity and thermal conductivity of AA3003 and AA4045

Material	Specific heat capacity/(J·kg ⁻¹ ·K ⁻¹)					Thermal conductivity/(W·m ⁻¹ ·K ⁻¹)				
	298 K	773 K	916 K	927 K	1073 K	298 K	773 K	916 K	927 K	1073 K
AA3003	900	1112	1150	1167	1167	136.1	155.4	151.6	61.1	60.9
AA4045	298	573	851	862	1073	298	573	851	862	1073
	885	1116	1350	1128	1128	141.3	188.5	172.0	57.0	61.0

between the two regions was automatically satisfied in ANSYS Mechanical.

As illustrated in Fig. 2(b), when the flow field and thermal field of the casting process were solved, the boundary conditions were described as below.

1) Inlet and outlet boundaries

The velocity boundary condition was used in the region. The turbulence kinetic energy and its dissipation rate were set as follows:

$$k_{\text{inlet}} = 0.01u_{\text{inlet}}^2; \quad \varepsilon_{\text{inlet}} = \frac{k_{\text{inlet}}^{1.5}}{R_{\text{inlet}}};$$

$$k_{\text{outlet}} = 0; \quad \varepsilon_{\text{outlet}} = 0 \quad (9)$$

where R_{inlet} is the hydraulic radius of the inlet. The temperatures at the inlet and outlet boundaries were set as the pouring temperature and room temperature, respectively.

2) Mold cooling boundary

The velocity and turbulence boundary conditions were set as the static wall. The heat transfer on the outer surface of the clad composite hollow billet in the mold was modeled with the Neumann boundary condition:

$$-k \frac{\partial T}{\partial n} = \bar{q} \quad (10)$$

In the mold cooling region, heat was extracted through the mold and carried away by the cooling water in the copper jacket. Therefore, the average heat flux can be obtained by

$$\bar{q} = \frac{Q_w C_w \Delta T_w}{A} \quad (11)$$

where \bar{q} is the average heat flux, Q_w is the cooling water quantity, C_w is the specific heat of water, ΔT is the temperature difference and A is the effective cooling area.

3) Water cooling boundary

The water cooling boundary condition used in the current model is based on the empirical model of Weckman and Niessen [32]. The forced convection and nucleate boiling effects are estimated for a turbulent water film, and the heat transfer coefficient in water cooling zone is given as follows:

$$h = \begin{cases} (-1.67 \times 10^5 + 704\bar{T})Q^{1/3} + \frac{20.8}{\Delta T}(\Delta T_x)^3, \\ \text{nucleate boiling} \\ (-1.67 \times 10^5 + 704\bar{T})Q^{1/3}, \text{ forced convection} \end{cases} \quad (12)$$

where h is the heat transfer coefficient in water cooling zone; \bar{T} is the average temperature of water; ΔT is the temperature difference between the billet surface and the cooling water; ΔT_x is the difference between the ingot surface temperature and the water saturation temperature (at this temperature, 373 K, the cooling water will boil

off the surface of the clad composite hollow billet); and Q is the water flow rate.

4) Air cooling boundary

The velocity and turbulence boundary conditions were treated as the moving wall, and its moving velocity was the casting speed. The heat transfer coefficient in the air cooling zone was given as follows:

$$h_{\text{air}} = \sigma \varepsilon_b T^3 \quad (13)$$

where σ is the Stefan–Boltzmann constant, ε_b is the blackness of the clad composite hollow billet surface and T is the temperature of the clad composite hollow billet surface.

The AA3003/AA4045 interface was modeled as a zero-thickness layer with a discontinuous change in material properties. Momentum and energy are conserved across the interface; however, no mass transfer is allowed. The boundary conditions of the rest of the walls were treated as those of a static adiabatic wall.

5 Results and discussion

5.1 Electromagnetic field, fluid flow and thermal field

Figure 3 presents a comparison of the calculated and experimental results of the magnetic flux density at the outer wall of the graphite exterior mold under various currents. As observed in Fig. 3, there is a good agreement between the calculated and the measured results, and the maximum relative error is smaller than 7.5%.

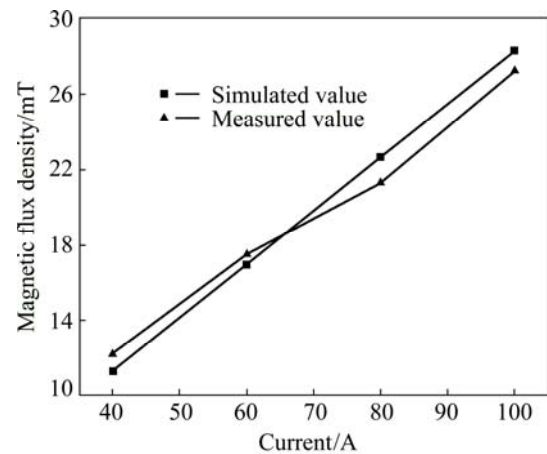


Fig. 3 Comparison of calculated and measured magnetic flux densities at outer wall of graphite mold under various current with $f=50$ Hz

The simulated results for the magnetic flux density and the Lorenz force in the x - y plane ($z=120$ mm) are presented in Figs. 4(a) and (b), respectively. As can be observed, the vector of the Lorenz force varies periodically with a vortex configuration and points from each magnetic pole to the center zone, and the direction

of the Lorenz force is always perpendicular to the direction of the magnetic flux density. Figures 4(c) and (d) present the numerical results for the magnetic flux density and Lorenz force in the y - z plane ($x=0$), respectively. Because of the skin and edge effects of the alternative electromagnetic field, the maximum values of the magnetic flux density and Lorenz force emerge on the billet surface near the center of the electromagnetic stirrer and decrease from the center to both sides along the axial z -direction.

Figure 5 shows the magnetic flux density and Lorenz force distribution along the radial y -direction ($x=0, z=120$ mm) and the axis z -direction ($x=0, y=43$ mm)

of the clad hollow composite billet, respectively. The magnetic flux density and Lorenz force are observed to vary sharply near the outer wall and smoothly near the inner wall of the clad composite hollow billet in Fig. 5(a). Figure 5(b) demonstrates that both the magnetic flux density and Lorenz force exhibit the typical jump near the center of the electromagnetic stirrer, which appears as a sharp hill in the axial z -direction. The maximum magnetic flux density and Lorenz force reach 23 mT and 1.9×10^4 N/m³, respectively.

Figure 6 presents the calculated results for the flow field. Velocity vectors with an isotherm in the y - z plane ($x=0$) without REMS and with REMS are shown in

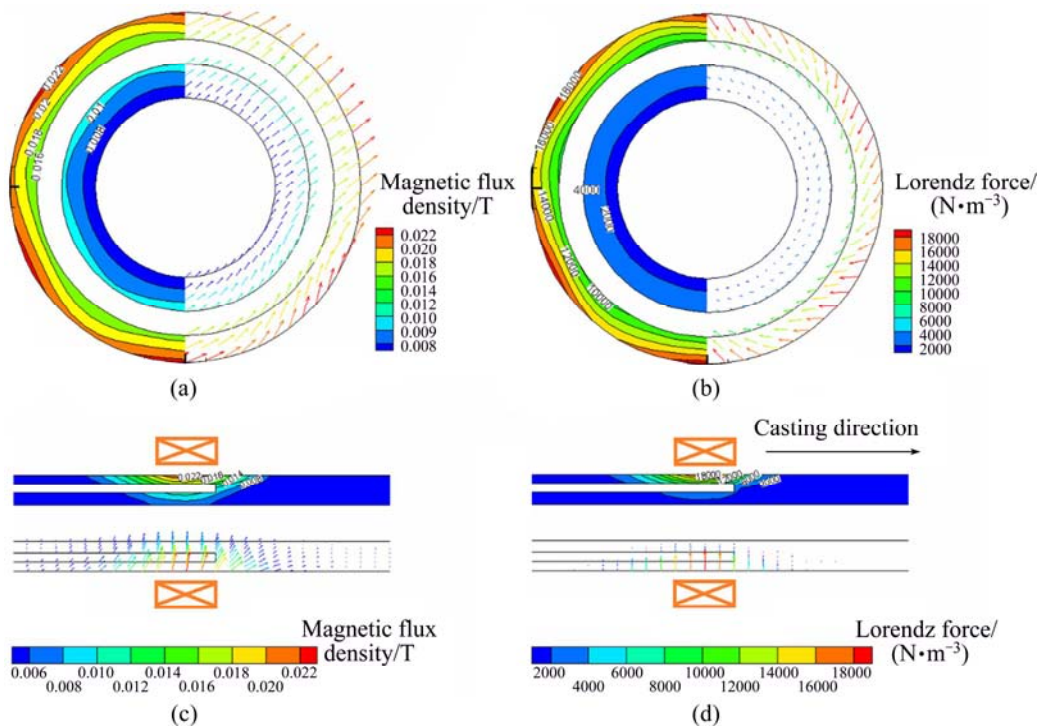


Fig. 4 Calculated results of electromagnetic field with REMS: (a) Magnetic flux density contours and vectors in x - y plane ($z=120$ mm); (b) Lorenz force density contours and vectors in x - y plane ($z=120$ mm); (c) Magnetic flux density contours and vectors in y - z plane ($x=0$); (d) Lorenz force density contours and vectors in y - z plane ($x=0$)

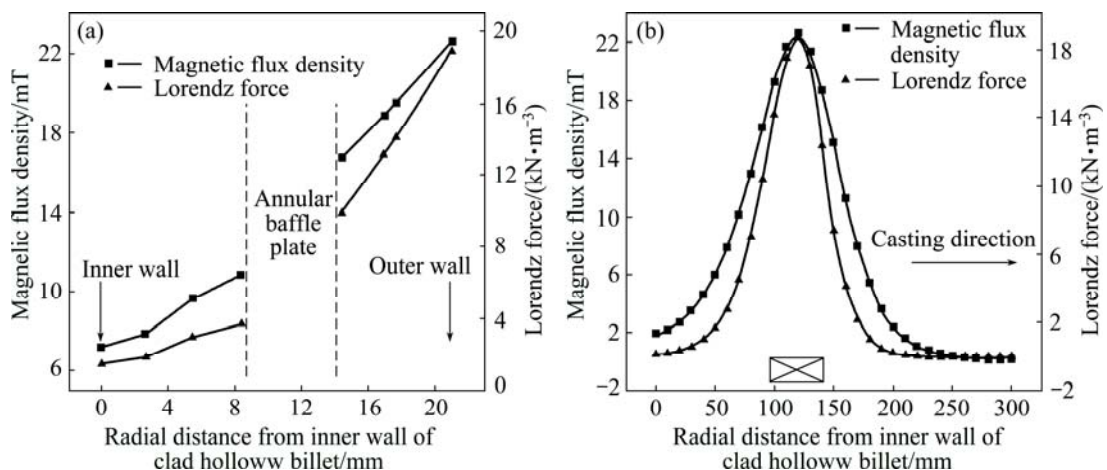


Fig. 5 Distribution of magnetic flux density and Lorenz force along radial y -direction ($x=0, z=120$ mm) (a) and axial z -direction ($x=0, y=43$ mm) (b) of clad composite hollow billet with REMS

Figs. 6(a) and (b), respectively. Without REMS, the liquid melt velocities of both the internal and external layer are relatively small, and the melt flow direction is approximately parallel to the centerline of the clad composite hollow billet. However, with REMS, the velocities of the internal and external melt stream both have horizontal and large vertical components in the $y-z$ plane ($x=0$) due to the stirring action of the alternating magnetic field. Figure 7 presents the velocity profiles and vectors in the $x-y$ plane ($z=120$ mm) with REMS. The direction of the circulation is clockwise, and the maximum rotation velocities are observed to be 0.35 m/s and 0.25 m/s in the internal and external layer regions, respectively.

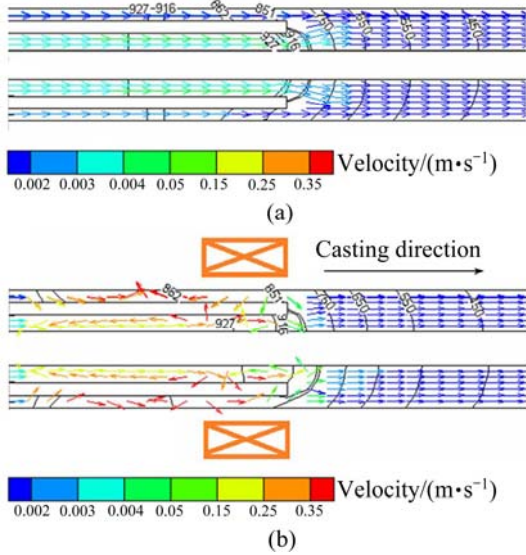


Fig. 6 Calculated results for flow field: velocity vectors with isotherm in $y-z$ plane ($x=0$): (a) Without REMS; (b) With REMS

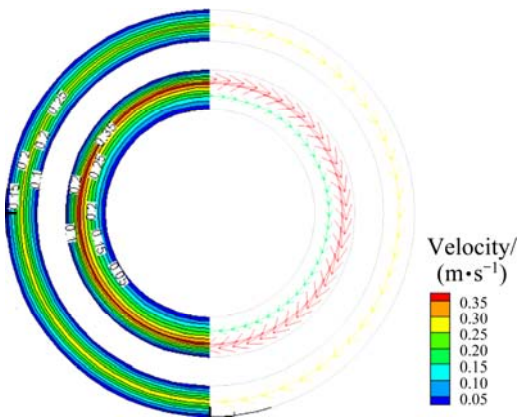


Fig. 7 Velocity profiles and vectors in $x-y$ plane ($z=120$ mm) with REMS

Figure 8 presents the temperature profiles without REMS and with REMS in the $y-z$ plane ($x=0$). Compared with the casting process without REMS, the

distribution of the temperature field is greatly modified with REMS. The mushy zone, which is defined as the zone between the solidus and liquidus, becomes much wider when REMS is applied. Figure 9 shows the effect of REMS on the axial depth and axial temperature gradient of the mushy zone during casting processes. The axial depth of the mushy zone for AA4045 of the external layer is increased from 20 to 58 mm, and the axial depth of the mushy zone for AA3003 of the internal layer is increased from 3 to 22 mm. The axial temperature gradient of the mushy zone for AA4045 of the external layer is decreased from 5.5 to 1.9 K/cm, and the axial temperature gradient of the mushy zone for AA3003 of the internal layer is decreased from 36.7 to 2.0 K/cm. The reason for the great modification of the temperature field is the vigorous forced convection induced by the electromagnetic stirring and the heat flux along the axial direction is increased due to the vigorous forced convection in the solidification front.

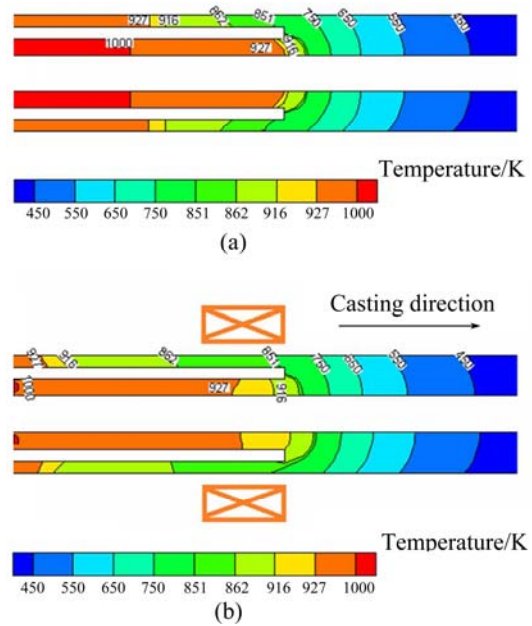


Fig. 8 Calculated temperature profiles without (a) and with (b) REMS in $y-z$ plane ($x=0$)

The liquid fraction profiles resulting from the temperature field distribution without and with REMS in the $y-z$ plane ($x=0$) are presented in Fig. 10. Figure 11 shows the predicted variations of the solid fraction in the middle of the interface of the clad composite hollow billet without and with REMS. As observed in Figs. 11(a) and (b), both the AA4045 of the external layer and the AA3003 of the internal layer are in semisolid form at the interface once the internal melt comes into contact with the external alloy, and then, the solid fractions of both sides start to increase and finally reach approximately 12 mm away from the baffle bottom due to the effects of the mold cooling.

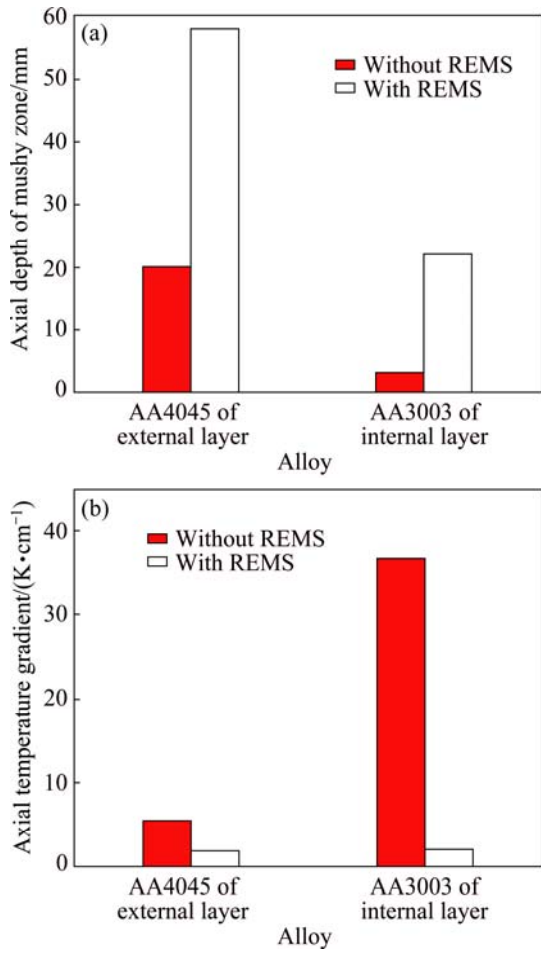


Fig. 9 Effect of REMS on axial depth (a) and axial temperature gradient (b) of mushy zone during casting process

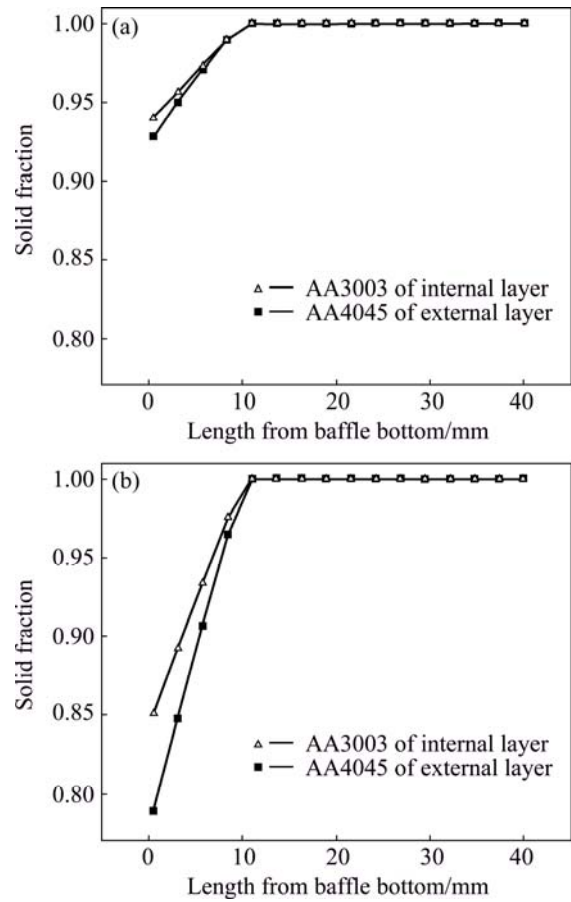


Fig. 11 Predicted variations of solid fraction in middle of interface of clad composite hollow billet without (a) and with (b) REMS

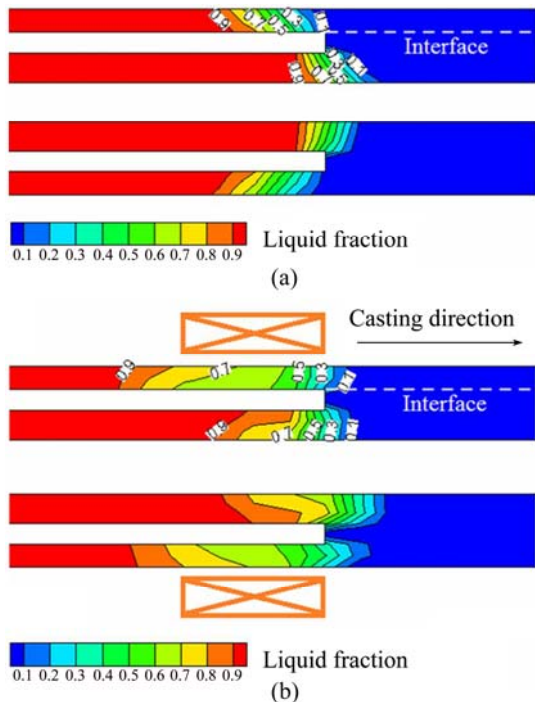


Fig. 10 Calculated liquid fraction profiles without (a) and with (b) REMS in y-z plane (x=0)

5.2 Macro/micro structures and bimetal interface

Figures 12(a) and (b) show the macrostructures of the clad composite hollow billets in cross section at a casting speed of 120 mm/min without and with REMS, respectively. Without REMS, the solidification macrostructure is inhomogeneous and consists of coarse columnar grains in the transverse section; however, with REMS, this macrostructure is homogeneous, and a very fine equiaxed grain structure is exhibited. From the present investigation, the main reasons are as follows. First, the mushy zone becomes much wider, and the temperature profile becomes more uniform, as illustrated in Figs. 9 and 10. Therefore, the heat flux along the axial direction is increased due to the vigorous forced convection induced by the electromagnetic stirring at the solidification front. Second, the uniform temperature field and low temperature gradient in the mushy zone with REMS increase the nucleation rate, which is one of the main reasons for the fine equiaxed grain structure of the clad composite hollow billet produced during the casting process with REMS. Third, due to the vigorous forced convection with REMS, as demonstrated in Figs. 6 and 7, the growing columnar dendrites are broken

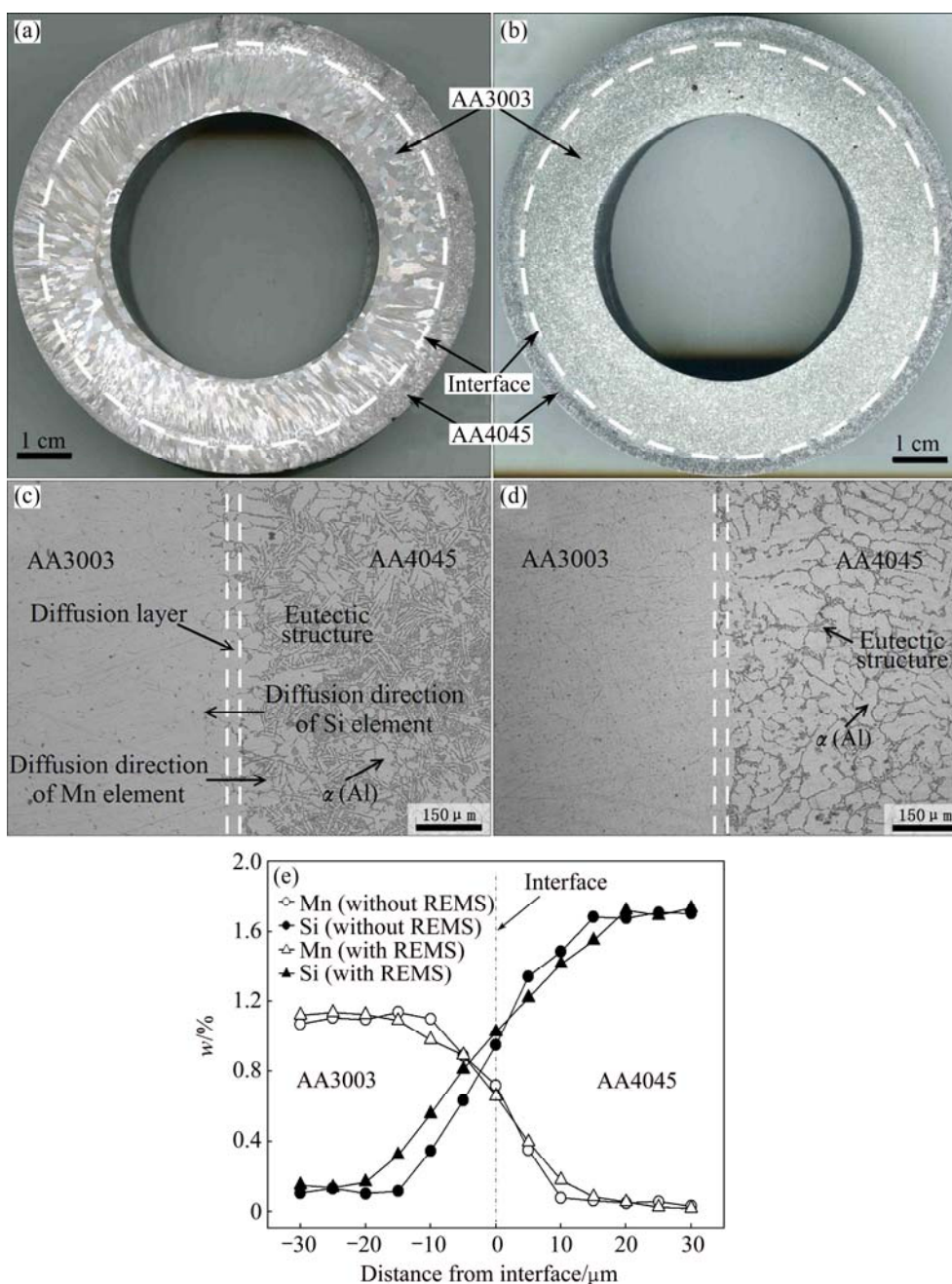


Fig. 12 Macrostructures of clad composite hollow billets in cross section without (a) and with (b) REMS, microstructure in interface zone without (c) and with (d) REMS and distribution of Si and Mn elements in interface zone (e)

and detached to form a large amount of debris around the solidification front. When this debris is detached in the mushy zone and moves within the mushy zone with the electromagnetic forced melt flow, each piece of debris will become a crystal nucleus. The debris will survive and not be remelted due to the uniform thermal field. Therefore, the crystallization occurs simultaneously in most of the mushy zone, and a fine and homogeneous structure over the entire cross section is obtained.

Figures 12(c) and (d) show the microstructure in the interface zone without and with REMS, respectively. As observed, REMS has little effect on the formation at the

interface of the clad composite hollow billet. However, the eutectic silicon phase shrinks in AA4045 with REMS, which can improve the mechanical properties of the AA4045 of the external layer.

Figure 12(e) shows the distribution of elements Si and Mn in the interface zone. The thickness of the diffusion layer of Si is greater than that of Mn because the diffusion coefficient of Si in Al is higher than that of Mn in Al under the same condition and the concentration gradient of Si atoms is higher than that of Mn atoms in the diffusion layer. Additionally, in comparing the two cases with and without REMS, the diffusion distance of

Si at the interface increases from 30 to 40 μm , and the diffusion distance of Mn at the interface increases from 20 to 30 μm . This is because the solid fractions of both the AA4045 of the external layer and the AA3003 of the internal layer at the interface during the casting process with REMS are smaller than those without REMS, as shown in Fig. 11, which will benefit element diffusion at the interface of the clad composite hollow billet.

6 Conclusions

1) The rotating electromagnetic stirring significantly changes the flow field and causes vigorous forced convection at the solidification front.

2) The axial depth of the mushy zone increases from 20 to 58 mm for AA4045 and from 3 to 22 mm for AA3003.

3) The axial temperature gradient of the mushy zone decreases from 5.5 to 1.9 K/cm for AA4045 and from 36.7 to 2 K/cm for AA3003.

4) With the rotating electromagnetic stirring, the microstructure of the clad composite hollow billet becomes fine and the diffusion of the elements at the interface is promoted.

References

- [1] ZHU Bo, LIANG Wei, LI Xian-rong. Interfacial microstructure, bonding strength and fracture of magnesium–aluminum laminated composite plates fabricated by direct hot pressing [J]. *Materials Science and Engineering A*, 2011, 528(21): 6584–6588.
- [2] ZHANG X P, YANG T H, CASTAGNE S, WANG J T. Microstructure, bonding strength and thickness ratio of Al/Mg/Al alloy laminated composites prepared by hot rolling [J]. *Materials Science and Engineering A*, 2011, 528(4–5): 1954–1960.
- [3] SATO Y S, PARK S H C, MICHUUCHI M, KOKAWA H. Constitutional liquation during dissimilar friction stir welding of Al and Mg alloys [J]. *Scripta Materialia*, 2004, 50(9): 1233–1236.
- [4] LIU Li-ming, LIU Xu-jing, LIU Shun-hua. Microstructure of laser-TIG hybrid welds of dissimilar Mg alloy and Al alloy with Ce as interlayer [J]. *Scripta Materialia*, 2006, 55(4): 383–386.
- [5] EIZADJOU M, MANESH H D, JANGHORBAN K. Investigation of roll bonding between aluminum alloy strips [J]. *Materials & Design*, 2008, 29(4): 909–913.
- [6] LLOYD D J. Recent developments in controlling the architecture for property optimization in Al-based materials [J]. *Scripta Materialia*, 2013, 68(1): 13–16.
- [7] WAGSTAFF R B, LLOYD D J, BISCHOFF T F. Direct chill casting of clad ingot [J]. *Materials Science Forum*, 2006, 519–521: 1809–1814.
- [8] GUPTA A, LEE S, WAGSTAFF R. Direct chill casting of aluminium–manganese against aluminium–silicon layer via Novelis fusion process [J]. *Materials Technology*, 2007, 22(2): 71–75.
- [9] SU Ya-jun, LIU Xin-hua, HUANG Hai-you, WU Chun-jing, LIU Xue-feng, XIE Jian-xin. Effects of processing parameters on the fabrication of copper cladding aluminum rods by horizontal core-filling continuous casting [J]. *Metallurgical and Materials Transactions B*, 2011, 42(1): 104–113.
- [10] FU Ying, JIE Jin-chuan, WU Li, PARK J, SUN Jian-bo, KIM J, LI Ting-ju. Microstructure and mechanical properties of Al–1Mn and Al–10Si alloy circular clad ingot prepared by direct chill casting [J]. *Materials Science and Engineering A*, 2013, 561: 239–244.
- [11] LIU Ning, JIE Jin-chuan, LU Yi-ping, WU Li, FU Ying, LI Ting-ju. Characteristics of clad aluminum hollow billet prepared by horizontal continuous casting [J]. *Journal of Materials Processing Technology*, 2014, 214(1): 60–66.
- [12] VIVES C. Hydrodynamic, thermal and crystallographical effects of an electromagnetically driven rotating flow in solidifying aluminum-alloy melts [J]. *International Journal of Heat and Mass Transfer*, 1990, 33(12): 2585–2598.
- [13] DONG Jie, CUI Jian-zhong, ZENG Xiao-qing, DING Wen-jiang. Effect of low-frequency electromagnetic field on microstructures and macro segregation of ϕ 270 mm DC ingots of an Al–Zn–Mg–Cu–Zr alloy [J]. *Materials Letters*, 2005, 59(12): 1502–1506.
- [14] GANAPATHYSUBRAMANIAN B, ZABARAS N. On the control of solidification using magnetic fields and magnetic field gradients [J]. *International Journal of Heat and Mass Transfer*, 2005, 48(19–20): 4174–4189.
- [15] YASUDA H, TOH T, IWAI K, MORITA K. Recent progress of EPM in steelmaking, casting, and solidification processing [J]. *ISIJ International*, 2007, 47(4): 619–626.
- [16] SHYY W, PANG Y, HUNTER G B, WEI D Y, CHEN M H. Modeling of turbulent transport and solidification during continuous ingot casting [J]. *International Journal of Heat and Mass Transfer*, 1992, 35(5): 1229–1245.
- [17] NASTAC L, STEFANESCU D M. Stochastic modelling of microstructure formation in solidification processes [J]. *Modelling and Simulation in Materials Science and Engineering*. 1997, 5(4): 391–420.
- [18] YOON J K. Applications of numerical simulation to continuous casting technology [J]. *ISIJ International*, 2008, 48(7): 879–884.
- [19] CHEN Jian, YAN Wen, LI Wei, MIAO Jian, FAN Xin-hui. Texture evolution and its simulation of cold drawing copper wires produced by continuous casting [J]. *Transactions of Nonferrous Metals Society of China*, 2011, 21(1): 152–158.
- [20] LUDWIG A, KHARICHA A, WU Meng-huai. Modeling of multiscale and multiphase phenomena in materials processing [J]. *Metallurgical and Materials Transactions B*, 2014, 45(1): 36–43.
- [21] BASERINIA A R, CARON E J F R, WELLS M A, WECKMAN D C, BARKER S, GALLERNEAULT M. A numerical study of the direct-chill Co-casting of aluminum ingots via fusionTM technology [J]. *Metallurgical and Materials Transactions B*, 2013, 44: 1017–1029.
- [22] FOROOZMEHR E, ESMAEILI S, LLOYD D J, GALLERNEAULT M. Modeling of solutionizing and solute redistribution in a Co-cast Bi-layer Al alloy system [J]. *Metallurgical and Materials Transactions A*, 2012, 43(6): 1770–1780.
- [23] ZHU Shou-jun, REN Zhong-ming, DENG Kang, JIANG Guo-chang. Numerical simulation of alternative horizontal levitation electromagnetic continuous casting [J]. *Transactions of Nonferrous Metals Society of China*, 1996, 6(4): 42–46.
- [24] KIM D S, KIM W S, CHO K H. Numerical simulation of the coupled turbulent flow and macroscopic solidification in continuous casting with electromagnetic brake [J]. *ISIJ International*, 2000, 40(7): 670–676.
- [25] ZHANG Z F, KIM J M, HONG C P. Numerical simulation of grain structure evolution in solidification of an Al–5.0wt%Cu alloy under electromagnetic stirring and its experimental verification [J]. *ISIJ International*, 2005, 45(2): 183–191.
- [26] ZHANG Hai-tao, NAGAUMI H, ZUO Yu-bo, CUI Jian-zhong. Coupled modeling of electromagnetic field, fluid flow, heat transfer and solidification during low frequency electromagnetic casting of 7XXX aluminum alloys. Part 1: Development of a mathematical

- model and comparison with experimental results [J]. *Materials Science and Engineering A*, 2007, 448(1): 189–203.
- [27] MA Xiao-ping, YANG Yuan-sheng, WANG Bin. Effect of pulsed magnetic field on superalloy melt [J]. *International Journal of Heat and Mass Transfer*, 2009, 52(23–24): 5285–5292.
- [28] LI J, WANG T, XU J, YAN Z, SUN J, CAO Z, LI T. Simulation study on horizontal continuous casting process of copper hollow billet under rotating electromagnetic stirring. Part 1: Model description and primary results [J]. *Materials Science and Technology*, 2011, 27(3): 676–683.
- [29] CHAUDHARY R, THOMAS B G, VANKA S P. Effect of electromagnetic ruler braking (EMBr) on transient turbulent flow in continuous slab casting using large eddy simulations [J]. *Metallurgical and Materials Transactions B*, 2012, 43(3): 532–553.
- [30] LIU Ning, JIE Jin-chuan, SONG Xiao-yang, ZHANG Peng-chao, LI Ting-ju. Preparation of bilayer hollow billets by horizontal electromagnetic continuous casting [J]. *Materials Research Innovations*, 2013, 17(3): 207–211.
- [31] CARON E J F R, PELAYO R E O, BASERINIA A R, WELLS M A, WECKMAN D C, BARKER S, GALLERNEAULT M. Direct-chill Co-casting of AA3003/AA4045 aluminum ingots via fusion™ technology [J]. *Metallurgical and Materials Transactions B*, 2014, 45: 975–987.
- [32] WECKMAN D C, NIESSEN P. A numerical simulation of the D. C. continuous casting process including nucleate boiling heat transfer [J]. *Metallurgical Transactions B*, 1982, 13: 593–602.

电磁场下 AA3003/AA4045 铝合金 复层管坯水平连铸技术

武立¹, 康慧君², 陈宗宁², 刘宁¹, 王同敏¹

1. 大连理工大学 材料科学与工程学院, 三束材料改性教育部重点实验室, 大连 116024;
2. 大连理工大学 原材料特种制备技术实验室, 大连 116024

摘要: 采用数值模拟方法研究在电磁场下 AA3003/AA4045 铝合金复层管坯的水平连铸制备过程。为了考察电磁场对复层管坯水平连铸过程的影响, 建立一个三维分析模型并对有无施加电磁场时的两个水平连铸过程分别进行全面地模拟与分析。数值模拟结果表明: 施加旋转电磁搅拌后, 铝合金熔体的紊流作用增强, 糊状区的范围增大, 糊状区的温度梯度减小且温度场变得均匀, 铝合金熔体的固相率下降。这些改变有利于复层管坯组织的细化及复合界面元素的扩散。采用与数值模拟相同的工艺参数进行实验, 结果证实在电磁场作用下复层管坯组织得到细化并且复合界面的元素扩散作用增强。

关键词: 铝合金; 复层材料; 管坯; 水平连铸; 电磁搅拌; 数值模拟

(Edited by Xiang-qun LI)